Journal of Applied Fluid Mechanics, Vol. 18, No. 3, pp. 535-548, 2025.
Available online at www.jafmonline.net, ISSN 1735-3572, EISSN 1735-3645.
https://doi.org/10.47176/jafm.18.3.2865

Effect of Receiver Holes on Flow and Heat Transfer Characteristics in A Radial Pre-swirl System: A LES Study

D. Wang[1], C. Song[2], C. Qiu[1], W. Wang [3], Y. Xu [3] and P. I. Mihailovich[1†]

[1] *Faculty of Aircraft, Rocket Engines and Power Plants, Moscow Aviation Institute, Moscow 125080, Russia*
[2] *Faculty of Aerospace, Moscow Aviation Institute, Moscow 125080, Russia*
[3] *Faculty of Aircraft Engineering, Moscow Aviation Institute, Moscow 125080, Russia*

†*Corresponding Author Email: platonov@mai.ru*

ABSTRACT

As a necessary component of a turboshaft engine, optimizing components in the radial pre-swirl system is critical for improving turbine performance. The aim of this study was to investigate the impact of receiver holes on the flow and heat transfer characteristics of various components in the pre-swirl system. Large-eddy simulations were used to demonstrate the phenomenon that the different receiver hole tangential angles have a significant influence on the performance of the radial pre-swirl system. In addition, a mathematical model was developed to predict the relative total pressure and temperature inside the co-rotating cavity. It is observed that the relative total pressure of computational model with receiver hole tangential angle equals to 15° is 21.88% and 18.54% larger than that of the computational model with receiver hole tangential angles equals to 0° and 7.5°as a result of the increase in swirl ratio. A larger swirl ratio resulted in a stronger centrifugal supercharging effect and jet acceleration effect. Furthermore, the Nusselt number and the field synergy angle exhibited an upward and downward trend, respectively. Subsequently, an investigation of unsteady characteristics designed to reveal the vortex state inside the co-rotating cavity was carried out. The mathematical model's prediction result matched the LES result closely, demonstrating its practical significance.

Article History

Received June 2, 2024
Revised September 9, 2024
Accepted September 21, 2024
Available online January 1, 2025

Keywords:

Aeroengine
Radial pre-swirl system
Pressure drop
Temperature drop
Nusselt number
Coherent structure

1. INTRODUCTION

As the thermal cycle efficiency improves, the turbine inlet temperature increases, posing a risk to the stable operation of the turbine blades (Ma et al., 2022; Unnikrishnan & Yang, 2022). However, when materials such as ceramic-based thermals are exposed to high pressure and temperatures, their lifespan is reduced (Zhang et al., 2016a; Ghasemi et al., 2022; Ostadhossein & Hoseinzadeh, 2024). To avoid negative effects, a radial pre-swirl system is typically used to supply direct airflow to the cooling turbine blades.

A typical radial pre-swirl system containing pre-swirl nozzles, receiver holes, a co-rotating cavity, and supply holes is shown in Fig. 1. The airflow was first absorbed from the high-pressure compressor cavity and delivered to the pre-swirl cavity using pre-swirl nozzles. Lewis et al. (2009) conducted numerical simulations to show how the radial location of pre-swirl nozzles affects the performance of a pre-swirl system. Six different tangential angles were used to perform a comparison in the research

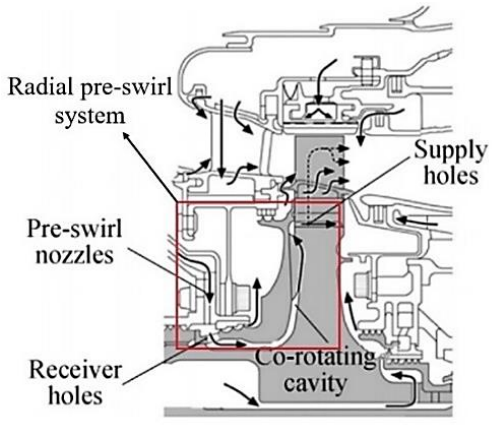

Fig. 1 Schematic of the radial pre-swirl system

of Zhang et al. (2016b), which indicated that the tangential angles of the pre-swirl nozzles significantly affected the performance of the pre-swirl system and heat transfer characteristics. Furthermore, a distinct pressure drop occurs in the case of stator-rotor interference and the

acceleration effect in the region of the pre-swirl cavity (Liao et al., 2014; Da Soghe et al., 2018; Liu et al., 2021). It is worth noting that the difference in tangential angles between receiver holes influences the upstream flow field as well.

In the co-rotating cavity, a radial outflow towards the supply holes developed. The flow field inside a co-rotating cavity with the radial flow is typically divided into four parts: the source region, Ekman layer, core region, and sink region (Hide, 1968). This flow structure was first confirmed by Owen & Pincombe (1980), and Owen et al. (1985) using flow visualization and laser Doppler anemometry. Firouzian et al. (1986) measured the velocity, pressure drop, and heat transfer in rotating cavities with a radial inflow. Previous studies have developed dozens of varied structures to maintain the pressure of radial inflow cavities (Chew et al., 1989; Farthing & Owen, 1991; Farthing et al., 1991; Wei et al., 2019, 2020), the stability of the radial swirl flow has been studied by Dou (2022). Furthermore, Shen & Wang (2022) conducted a large eddy simulation (LES) study of turbine disks with impellers, which revealed an increase in centrifugal pressure as well as a vortex-breaking phenomenon within the impeller channel. They observed that pressure and temperature changes in cavities with radial flow are proportional to changes in the swirl ratio (Shen et al., 2023). Therefore, it is of practical engineering value to investigate the effect of the inlet swirl ratio variation in the co-rotating cavity on the performance of the pre-swirl system.

Temperature is an essential parameter in radial pre-swirl systems. Chew & Rogers (1988) used an extended integral method of the momentum equation to study the temperature distribution in a symmetrically heated rotating cavity. Liao et al. (2015) numerically investigated the flow and heat transfer characteristics in a rotor-stator disk cavity and observed that the heat transfer coefficient and Nusselt number (Nu) increased as the rotational Reynolds number increased. Lin et al. (2022) performed a theoretical derivation to fully elaborate the multifactor-influencing mechanisms of a turbine disc cavity using similarity criteria and dimensional analysis. Furthermore, they conducted high-rotational-speed experiments to demonstrate the main correlation factors influencing disk cavity system performance. A prediction model for temperature in both the compressor and turbine disks, as well as constructed Bayesian models, was developed by Cao et al. (2022) and Tang et al. (2022) to display the temperature distribution for the first time. To improve heat transfer performance, Ma et al. (2021, 2022) proved the feasibility of increasing cooling efficiency using twin-web turbine disks.

However, few studies have focused on pre-swirl systems with outflow co-rotating cavities. This study used a large-eddy simulation method to investigate the turbulence and heat transfer within a radial pre-swirl system with a co-rotating cavity. The matching problem between receiver holes, pre-swirl nozzles, and co-rotating cavities was also analyzed. Furthermore, a theoretical analysis was conducted, and a mathematical model of the relative pressure and temperature was developed.

The remainder of this paper is organized as follows: The computational models and methods are described in Section 2. A theoretical analysis is performed by deducing the mathematical model in Section 3. The LES results are discussed in Section 4. Finally, the conclusions of this study are summarized in Section 5.

2. COMPUTATIONAL PROCEDURE

2.1 Computational Model and Boundary Conditions

Multiple numerical simulations were performed using ANSYS FLUENT. During the computational procedure, the model was appropriately simplified while disregarding the sealing structure.

The computational model is divided into two fluid domains based on the actual situation. The first domain is the static domain, which comprises the inlet cavity and pre-swirl nozzle. In this region, the airflow completes the pre-swirl process and generates a circumferential velocity. The second domain is the rotating domain, which comprises the receiver holes, a co-rotating cavity, and supply holes, where the airflow velocity transitions from axial to radial. The middle section of the pre-swirl cavity serves as an interface between the stationary and rotating domains of the calculation model.

To conserve computational resources, 1/6 of the periodicity of the original physical model was selected as the computational model, as shown in Fig. 2 (a). In total, there are four pre-swirl nozzles, eight receiver holes, and eight supply holes in the computational model. In this study, tube-shaped receiver holes were used, and the tangential angle (θ_r) is as shown in Fig. 2 (b). Only θ_r is a variable geometric parameter; it has three variants, that is, 0°, 7.5°, and 15°, respectively. The geometric parameters of the computational model are shown in Fig. 2(c) and are simplified using the dimensionless representation method, which relies on the radial height r_s where the air supply holes are positioned. The numerical values are listed in Table 1.

A compressible, viscous ideal gas was selected as the working fluid in this study. The pressure inlet boundary condition was set at the inlet cavity, and the outlet located at the supply holes was set as the outlet with a flow rate. All the walls, except for the periodic surfaces, were set as no-slip walls. A heat flux (q_w) was applied specifically to the walls of the co-rotating cavity to restore practical engineering conditions. In addition, none of the other

Table 1 Dimensionless geometric parameters

Dimensionless geometric parameters	Value
D_n/r_s	0.017
L_n/r_s	0.016
S/r_s	0.049
b/r_s	1.072
L_r/r_s	0.025
D_r/r_s	0.039
D_s/r_s	0.025
L/r_s	0.358

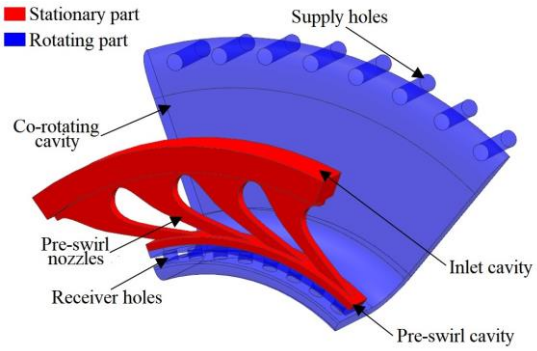

(a) Calculation model.

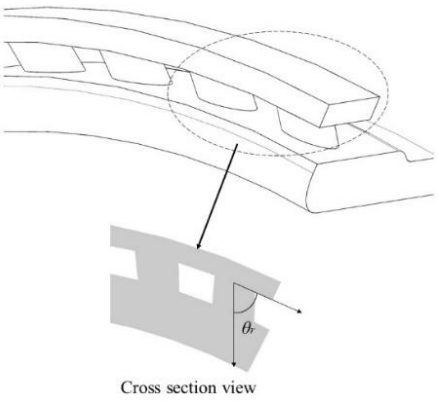

(b) Tangential angle of the receiver holes

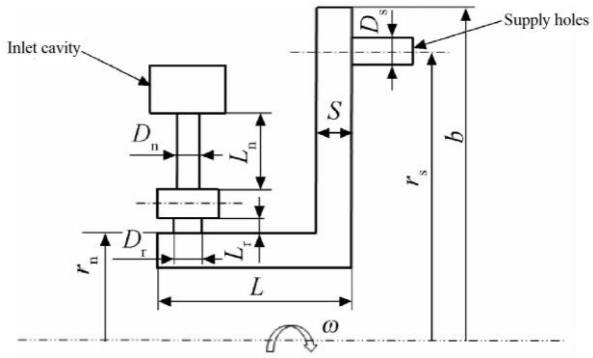

(c) Geometric parameters of baseline model

Fig. 2 Structural parameters of the radial pre-swirl system

Table 2 Boundary conditions

Inlet	Total pressure (MPa)	222915
	Static temperature (K)	296
Outlet	Mass flow rate (kg/s)	0.005
Rotate velocity of rotating part (rev/min)		1500
Heat flux (W/m^2)		6000

walls experienced a heat flux. Furthermore, a spectral synthesizer method was adopted to confirm the specifications of the inlet turbulence. The turbulent intensity and length scale were set to 5% and 0.1 mm, respectively. All boundary conditions are listed in detail in Table 2.

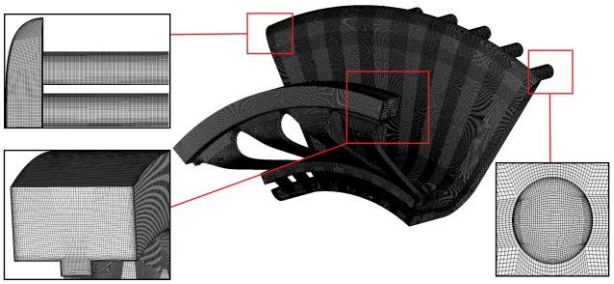

Fig. 3 Schematic of computational model structured mesh

2.2 Method and Mesh

The subgrid model in this study is the wall adapting local eddy-viscosity model (WALE), in which eddy viscosity (μ_t) is defined as follows:

$$\mu_t = \rho L_s^2 \frac{\left(S_{ij}^d S_{ij}^d\right)^{3/2}}{\left(\bar{S}_{ij}\bar{S}_{ij}\right)^{5/2} + \left(S_{ij}^d S_{ij}^d\right)^{5/4}} \tag{1}$$

where ρ denotes density, and mixing length for subgrid scales (L_s) and the rate of strain tensor for the resolved scale (S_{ij}^d) are defined, respectively, as follows:

$$L_s = min(\kappa d, C_w V^{1/3}) \tag{2}$$

$$S_{ij}^d = \frac{1}{2}\left(\bar{g}_{ij}^2 + \bar{g}_{ji}^2\right) - \frac{1}{3}\delta_{ij}\bar{g}_{kk}^2, \bar{g}_{ij} = \frac{\partial \bar{u}_i}{\partial x_j} \tag{3}$$

where κ denotes the Von Carman constant equal to 0.41, d denotes the distance to the closest wall, C_w denotes the WALE constant equal to 0.5, and V denotes the mesh volume (Bricteux et al., 2009).

The structural mesh method was employed in this study to satisfy the requirements of the LES simulation. The mesh of the entire computational model and details of the stationary and rotating parts are shown in Fig. 3.

The thickness of the first layer was set at 0.01 mm, and the global maximum element was set at 0.25 mm. A test simulation under the aforementioned operating conditions was conducted to solve the x+, y+, and r+ values, which were approximately 1, 46, and 50, respectively, satisfying the LES requirements. Moreover, to ensure reliable simulation results, the time step was determined based on the criterion of ensuring a Courant-Friedrich-Levy (CFL) number of less than one. The CFL number (C) is defined in Eq. (4) as follows:

$$C = a\frac{dt}{dx} \tag{4}$$

where a denotes the mainstream velocity magnitude, dx denotes the distance between the mesh elements, and dt denotes the time step. The time step is determined as 10^{-5} s. Furthermore, a grid independence verification is performed, and the result is listed in Table 3. It can be concluded that when the number of grid elements reaches 20618349, the changes in the relative total pressure and temperature at the outlet can be neglected. A total of 20618349 grid elements are used in this study.

Table 3 Grid independence verification

Grid number	Relative total pressure (Pa)	Relative total temperature (K)
11037240	2.205e+5	325.8
16173485	2.207e+5	327.4
20618349	2.207e+5	327.6

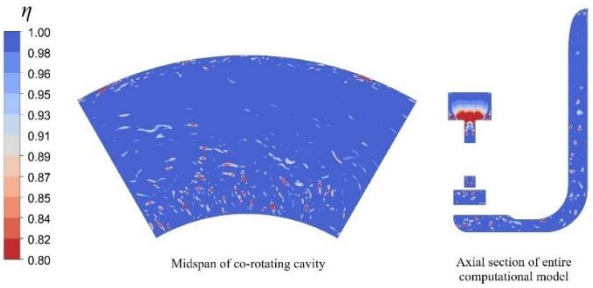

Fig. 4 Distribution of η in two sections

2.3 Verification

To perform LES reliably, the mesh must be validated to determine whether the subgrid model can represent the flow motion on an unresolved scale. Subgrid-scale kinetic energy (k_{sgs}) dissipation is widely used to evaluate the performance of LES simulations (Vreman et al., 1997). A common criterion is the rate (η) between resolved kinetic energy (k_{res}) and total kinetic energy which equals the summary of k_{sgs} and k_{res}. When η > 0.8, we can detect that the mesh quality satisfies the requirements of the LES simulation. The η distribution on the axial section of the entire computational model and the midspan of co-rotating cavity is shown in Fig. 4. Observably, η in the most area of the computational model is more than 0.8; hence, the mesh quality satisfies the requirements of LES.

A test is conducted to validate the accuracy and reliability of the simulated data. Because of the high similarity of the computational models and operating conditions between this study and that of Kong et al. (2022), the experimental data in their study were cited for validating the mesh and LES methods. An additional computational model was established based on the details of their research. The boundary conditions of this test were identical to those used in their study. The mesh and simulation methods applied in this test were consistent with those used in our study. The static pressure coefficient ($C_{pressure}$) is expressed as follows:

$$C_{pressure} = \frac{p - p_1}{\frac{1}{2}\rho\omega^2 x_1^2} \tag{5}$$

where p_1 represents the static inlet pressure of the computational model, ω represents the angular velocity, and x_1 represents the radial inlet location. The simulation results of this test were used for comparison, as shown in Fig. 5. In this test, the turbulent flow parameter was defined as $\lambda_T = C_w \cdot Re_\phi^{-0.8}$, where C_w is a dimensionless mass flow rate and Re_ϕ is the rotational Reynolds number.

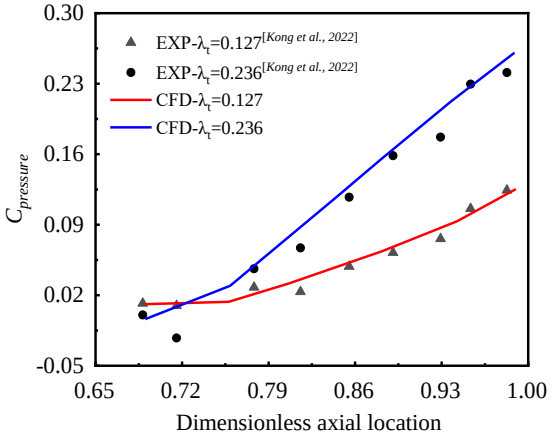

Fig. 5 Comparison of simulation result and experimental data

The dimensionless axial location was equal to the actual axial location divided by the total axial distance between the upstream and downstream disk walls. The simulation results and experimental data are in good agreement.

3. THEORETICAL ANALYSIS

3.1 Dimensionless Parameters

The purpose of this study is to investigate a radial pre-swirl system with an outflow co-rotating cavity. This concentrates on the interaction between various components, particularly the impact of the receiver holes on the co-rotating cavity. Hence, a theoretical analysis of the flow and heat transfer characteristics in the co-rotating cavity was conducted. Before elaborating on the theoretical analysis, we first define the dimensionless parameters as follows:

$$Re_\phi = \frac{\rho\omega b^2}{\mu} \tag{6}$$

where μ denotes the dynamic viscosity coefficient. The dimensionless flow rate (C_m) is defined as follows:

$$C_m = \frac{m}{\mu b} \tag{7}$$

The swirl ratio (Sr) and dimensionless radial height (x) are defined as follows:

$$Sr = \frac{\bar{V}_\phi}{\omega r} \tag{8}$$

$$x = \frac{r}{b} \tag{9}$$

where $\bar{V}_\phi$ denotes the absolute angular velocity, r denotes the local radial height. Moreover Sr at the inlet of the co-rotating cavity is represented by c. The Rossby number is expressed as follows:

$$Ro = \left|\frac{\bar{V}_\phi - \omega r}{\omega r}\right| \tag{10}$$

When we substitute the definition formula of Sr into it, we can obtain:

$$Ro = |Sr - 1| \tag{11}$$

In addition. the Nusselt number (Nu) in this study is defined as follows:

$$Nu = \frac{q_w r}{k(T_w - T_0)} \tag{12}$$

where k denotes the thermal conductivity, T_w and T_0 denote the disk and reference temperatures, respectively.

3.2 Flow Structure

Inside the stationary domain, air was initially accelerated using pre-swirl nozzles to obtain a specific tangential velocity owing to the influence of the structures. Subsequently, air from the pre-swirl cavity flowed into the rotational domain through the receiver holes. During this period, the airflow velocity completed the transition from radial to axial orientation. During this process, a significant flow loss occurred because of the deterioration of the local flow field. The air then flowed into the co-rotating cavity through the channel between the receiver holes and the co-rotating cavity.

As mentioned in the first section of this study, the flow structure inside a rotating cavity with a radial outflow can be simplified, as shown in Fig. 6. It consists of a source region, an Ekman layer, a core region, and a sink region, where r_e denotes the stagnant boundary of the source region (Owen & Pincombe 1980, Owen et al. 1985). A high flow rate is required to satisfy the requirements for film cooling and sealing. Hence, the impact of the downstream disk wall on the flow was negligible. The incoming airflow collided with the downstream disk wall, formed a wall jet, and flowed upward along the radial direction. However, when the radial velocity of a portion of the flow dropped to zero, this portion began to move radially downwards and then towards the upstream disk wall. When these two air streams flowed radially upward along the disk walls, an Ekman layer and a core region were formed. It is noteworthy that the Ekman layer suction exerted a radical influence on the main body of the flow, which manifested as the radial velocity of the flow in the core region decreasing to zero and the tangential velocity being the primary component. Thus, in the region above the source region, air flowed radially outward, primarily through the Ekman layer (Hide, 1968). Finally, they converged at the inlets of the supply holes and formed a sink region.

3.2.1 Source Region

The flow inside the source region can be described as a free vortex that experiences no external torque and is theoretically relatively irrotational. Hence, the conservation of angular momentum is described as follows:

$$\bar{V}_\phi r = \bar{V}_{\phi,in} a \tag{13}$$

It can be used to calculate Sr, where $\bar{V}_{\phi,in}$ denotes the absolute tangential velocity at the inlet of the co-rotating cavity. Furthermore, Shen et al. (2023) highlighted that

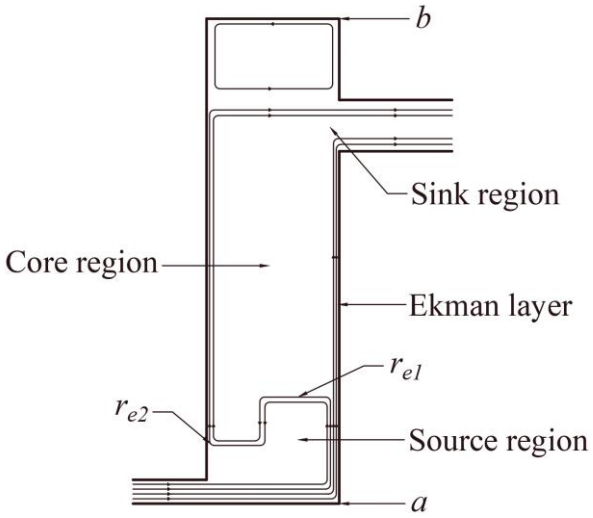

Fig. 6 Simplified flow structure in a rotating cavity with radial outflow

when the channel between the receiver hole region and the cavity was short, the Sr change along it could be neglected. Thus, c was recognized as equivalent to Sr at the outlet of the receiver holes. We merge Eqs. (8), (9), and (13) to yield

$$Sr = c\frac{x_a^2}{x^2} \tag{14}$$

where $x_a = \frac{a}{b}$.

3.2.2 Ekman Layer

The mass and momentum equations of the Ekman layer were first developed by Von Kármán, as follows (Kármán, 1921):

$$\frac{1}{r}\frac{\partial(rV_r)}{\partial r} + \frac{\partial(V_x)}{\partial X} = 0 \tag{15}$$

$$V_r\frac{\partial(V_r)}{\partial r} + V_x\frac{\partial(V_r)}{\partial X} - \frac{V_\phi^2}{r} = \frac{\partial\tau_r}{\rho\partial X} \tag{16}$$

$$V_r\frac{\partial(V_\phi)}{\partial r} + V_x\frac{\partial(V_\phi)}{\partial X} + \frac{V_\phi V_r}{r} = \frac{\partial\tau_\phi}{\rho\partial X} \tag{17}$$

where V_x, V_r, and V_ϕ denote the axial absolute velocity, radial absolute velocity, and tangential absolute velocity, respectively. τ_r and τ_ϕ denote the stress along the radial and tangential direction, respectively. Based on the hypothesis that Ro is continuously equal to one along the radial directions, the nonlinear part of the above formulas can be eliminated. Hence, a simplified version was obtained by Owen et al. (1985) as follows:

$$-2\omega(V_{\phi.r} - \bar{V}_{\phi.r}) = \frac{\partial\tau_r}{\rho\partial X} \tag{18}$$

$$2\omega V_r = \frac{\partial\tau_\phi}{\rho\partial X} \tag{19}$$

where $V_{\phi.r}$ and $\bar{V}_{\phi.r}$ denote the relative tangential velocity in the core region and Ekman layer, respectively. Owen et al. (1985) developed the following formulas to describe the distribution of relative velocity in the core region:

$$\frac{\bar{V}_{\phi.r}}{\omega r} = -2.22\lambda_T^{5/8} x^{-13/8} \tag{20}$$

We substituted the definition of $\bar{V}_{\phi.r}$ in equation (20) into Eq. (8), and the distribution of Sr in the core region can be described as follows:

$$Sr = 1 - 2.22\lambda_T^{5/8} x^{-13/8} \tag{21}$$

When the lower boundary of the core region coincides with the stagnant boundary of the source region, Eqs. (14) can be combined to solve x_e as follows:

$$cx_a^2 = x_e^2 - 2.22\lambda_T^{5/8} x_e^{3/8} \tag{21}$$

Although the variation in Ro introduces calculation errors, according to Shen et al. (2023), the linear Ekman layer equations could still match the actual situation under the condition of radial outflow in the rotating cavity. Thus, the following calculation was based on the linear Ekman layer equations. When the flow rate was relatively low, the Ekman layer and core region were generated inside the co-rotating cavity (Owen et al., 1985). However, because of the narrow disk interval and larger flow rate, only source regions were considered in this study. Hence, when deducing the prediction formula for the pressure drop, the source regions were considered exclusively. However, the proposed Sr distribution in the core region still provides the possibility for research under wider operating conditions.

3.3 Pressure Change

When the distance between the boundary layer and the measuring point is large, we can assume that the radial and axial velocities are negligible compared with the tangential velocities. Thus, there is:

$$\frac{dp}{\rho dr} = \frac{V_\phi^2}{r} \tag{22}$$

which denotes the static pressure gradient in the radial direction. By substituting Eq. (8) into Eq. (23) and integrating it, the expression for the static pressure change within the scope of the local radius from r_1 to r_2 is obtained as follows:

$$\Delta p = \int_{r_1}^{r_2} \rho r \omega^2 Sr^2 dr \tag{24}$$

Because the pressure change is exceedingly low inside a rotating cavity with radial outflow, the air inside it can appear incompressible (Shen et al., 2023). The formula above can be simplified further as follows:

$$\Delta p = \rho\omega^2 \int_{r_1}^{r_2} rSr^2 dr \tag{25}$$

When the source region is analyzed independently, the above formula can be rewritten by combining Eqs. (9) and (14) as follows:

$$\Delta p = \frac{\rho\omega^2 c^2 a^4}{2}\left(\frac{1}{r_1^2} - \frac{1}{r_2^2}\right) \tag{26}$$

Based on the same simplification principle, the relative dynamic pressure change (Δp_d) within the same region can be described as follows:

$$\Delta p_d = \frac{1}{2}\rho(V_{\phi,r2}^2 - V_{\phi,r1}^2) \tag{27}$$

The relative tangential velocity is defined as follows:

$$V_{\phi,r} = \bar{V}_\phi - \omega r \tag{28}$$

By substituting Eq. (8) into Eq. (28) and combining it with Eq. (27), the change in the relative dynamic pressure within this region is as follows:

$$\Delta p_d = \frac{1}{2}\rho\omega^2[(Sr_2 - 1)^2 r_2^2 - (Sr_1 - 1)^2 r_1^2] \tag{29}$$

Similarly, by substituting Eqn. (14), Δp_d in source region can be expressed as follows:

$$\Delta p_d = \frac{1}{2}\rho\omega^2\left[\left(c\frac{a^2}{r_2^2} - 1\right)^2 r_2^2 - \left(c\frac{a^2}{r_1^2} - 1\right)^2 r_1^2\right] \tag{30}$$

Finally, the relative total pressure change (Δp_{rel}^*) can be expressed as the summation of Δp_d and Δp as follows:

$$\begin{aligned}\Delta p_{rel}^* = \rho\omega^2 \int_{r_1}^{r_2} rSr^2 dr \\ + \frac{1}{2}\rho\omega^2[(Sr_2 - 1)^2 r_2^2 \\ - (Sr_1 - 1)^2 r_1^2]\end{aligned} \tag{31}$$

By combing Eq. (14) with Eq. (31), Δp_{rel}^* in the source region can be defined as a function relative to x, as follows:

$$\begin{aligned}\Delta p_{rel}^* = \frac{\rho\omega^2 c^2 a^4}{2b^2}\left(\frac{1}{x_1^2} - \frac{1}{x_2^2}\right) \\ + \frac{\rho\omega^2 b^2}{2}\left[\left(c\frac{x_a^2}{x_2^2} - 1\right)^2 x_2^2 \right. \\ \left. - \left(c\frac{x_a^2}{x_1^2} - 1\right)^2 x_1^2\right]\end{aligned} \tag{32}$$

3.4 Energy and Temperature Change

According to the first law of thermodynamics, the following equation is established:

$$q = h_2 - h_1 + \frac{V_{\phi,r2}^2 - V_{\phi,r1}^2}{2} + g(Z_2 - Z_1) + w_s \tag{33}$$

where h denotes the specific enthalpy, g denotes the gravitational acceleration, Z denotes the local altitude, and w_s denotes the shaft power, according to Eq. (34). While q is the specific heat calculated using Eq. (35) as follows:

$$w_s = -\int_{r_1}^{r_2} \omega^2 r dr \tag{34}$$

$$q = \frac{2\pi q_w (r_2^2 - r_1^2)}{m} \tag{35}$$

Merging Eq. (33–35), the temperature change can be expressed as follows:

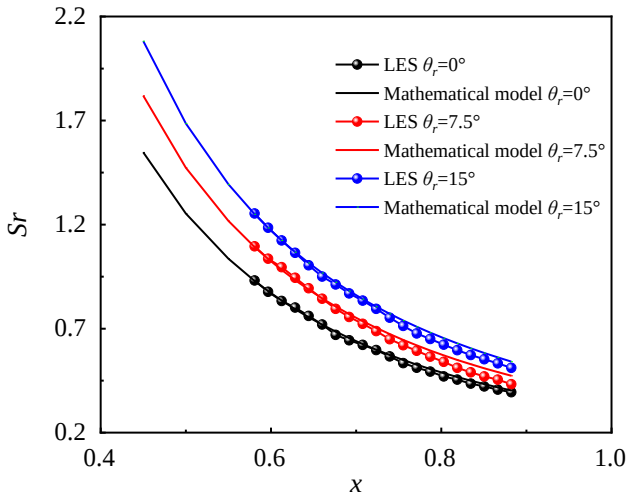

Fig. 7 Distribution of Sr along the radial direction

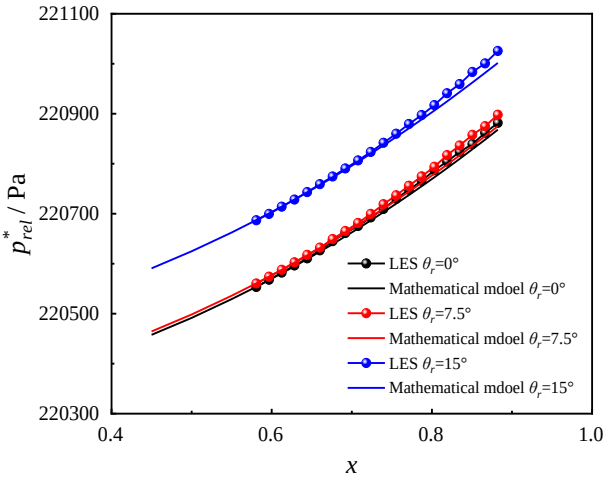

Fig. 8 Distribution of p^*_{rel} along the radial direction

$$\Delta T = \frac{2\pi b^2 q_w (x_2^2 - x_1^2)}{mC_p} - \frac{V_{\phi,r2}^2 - V_{\phi,r1}^2 + \omega^2 x_1^2 b^2 - \omega^2 x_2^2 b^2}{2C_p} \tag{36}$$

where C_p denotes the specific heat capacity under constant pressure. Substitute Eq. (8) into it, we obtain

$$\Delta T = \frac{2\pi b^2 q_w (x_2^2 - x_1^2)}{mC_p} - b^2 \cdot \frac{[(Sr_2 - 1)\omega x_2]^2 - [(Sr_1 - 1)\omega x_1]^2 + \omega^2 x_1^2 - \omega^2 x_2^2}{2C_p} \tag{37}$$

where Sr_2 and Sr_1 denote the swirl ratios at the outlet and inlet of the control volume, respectively. When we focus on the change of relative total temperature (ΔT^*_{rel}), the following formula is presented:

$$C_p \Delta T^*_{rel} = q - w_s \tag{38}$$

By combining the aforementioned equations and Eq. (9), ΔT^*_{rel} in the source region can be expressed as follows:

$$\Delta T^*_{rel} = \frac{\omega^2 x_2^2 b^2 - \omega^2 x_1^2 b^2}{2C_p} + \frac{2\pi b^2 q_w (x_2^2 - x_1^2)}{mC_p} \tag{39}$$

At this point, a mathematical model of the flow and heat transfer characteristics inside the co-rotating cavity for this study was completely established.

4. RESULTS AND DISCUSSION

4.1 Steady Characteristics

Figure 7 shows that the distribution of Sr along the radial direction within the scope of x varies from 0.6 to 0.9 in the co-rotating cavity. The prediction results of the mathematical model were in excellent agreement with the LES results. Principally, Sr decreased as the radial height increased in the three computational models because of the lack of an Ekman layer. The rate of the Sr decrease also decreased. Moreover, larger θ_r resulted in a larger tangential component of the airflow. Therefore, a positive correlation is observed between c and θ_r for both the mathematical model and LES result. Meanwhile, a larger c results in a larger decrease in Sr, according to Eq. (14). The computational model with θ_r=15° exhibits a 12.31% and 37.62% higher Sr decline compared to models with θ_r=7.5° and θ_r=0°.

Sufficient pressure is required to ensure effective film cooling. Hence, pressure is an important indicator in the investigation of pre-swirl systems. Figure 8 shows that the distribution of relative total pressure (p^*_{rel}) along the radial direction within the scope of x varies from 0.6 to 0.9 in the co-rotating cavity. It is shown that the prediction results from the mathematical model for all three computational models still remain highly consistent with the LES results. In general, p^*_{rel} increases as the radial height increases. Moreover according to Eq. (32), the growth rate of p^*_{rel} increases with the radial height. It is worth noting that, the initial value of p^*_{rel} experiences increases as θ_r increases. Figure 9 shows the distribution of p^*_{rel} within the three models. The Δp^*_{rel} in the receiver hole region of computational model with θ_r= 15° is lower than that of the other two models, which is consistent with the phenomenon mentioned above. When θ_r is relatively low, the development of the jet swirl ratio is constrained in both pre-swirl cavity and receiver holes, resulting in a larger local loss. When θ_r reaches 15°, the local flow field is improved and manifested as the increase in p^*_{rel}, which is 1.01% and 0.89% larger than that of the computation model with θ_r= 0° and 7.5°. Furthermore, the higher the Sr within the cavity, the higher is the absolute tangential velocity, which results in an increased centrifugal force and a more pronounced centrifugal supercharging effect. It is observed that the Δp^*_{rel} of computational model with θ_r =15° is 21.88% and 18.54% larger than that of the computational model with θ_r= 0° and 7.5°.

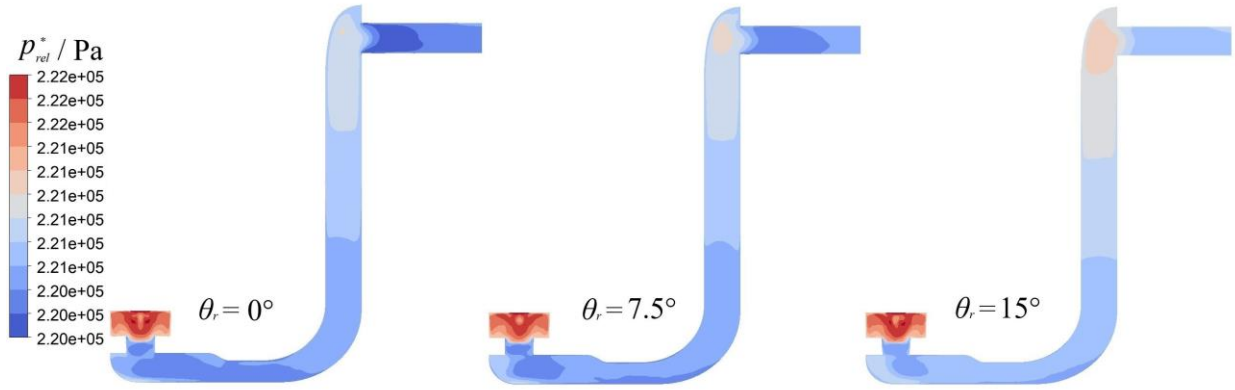

Fig. 9 Distribution of p^*_{rel} in section view of 3 models

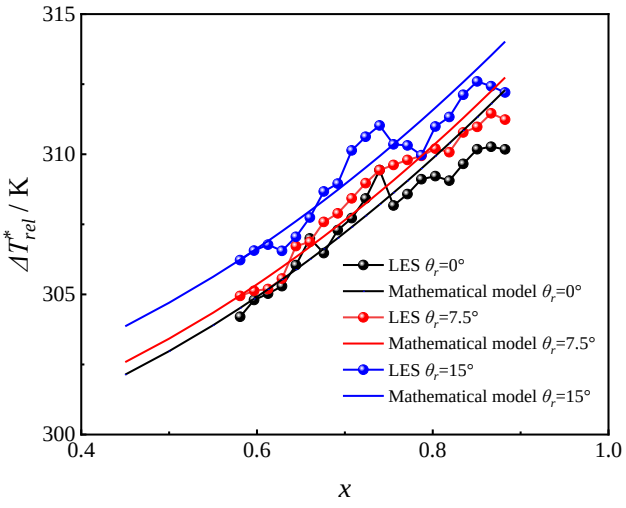

Fig. 10 Distribution of T^*_{rel} along the radial direction

Temperature is another indispensable evaluation index of pre-swirl system performance. Figure 10 shows the distribution of T^*_{rel} in the radial direction within the scope of x varies from 0.6 to 0.9 in the co-rotating cavity. The LES results fluctuated around the prediction results of the mathematical models, however their average values were approximately equivalent. Owing to the heat flux on the cavity walls, T^*_{rel} exhibited an upward trend as the radial height increased. The heat transfer process is a complex phenomenon that involves both free and forced convection effects inside a rotating cavity. For a small disk gap ratio, the rotational effect dominates the heat transfer effectiveness (Long, 1994). Owing to the existence of boundary layers, the distribution of Sr along the axial direction was uneven.

This causes a chaotic temperature distribution. The direct heating of the cavity walls and the vortex-breaking phenomenon inside the cavity also contributed to the formation of temperature fluctuations. Further observations of Fig. 10 show that the initial T^*_{rel} increases as θ_r rises. The reason is that larger θ_r improves the acceleration effect of jet both from the pre-swirl nozzles and receiver holes. In addition, because the tangential components of the jets were enhanced, a smaller decrease in T^*_{rel} occurred when the coordinates changed from static to rotational. Since shaft power and q_w are equivalent, ΔT^*_{rel} of three models are uniform.

Based on the field synergy principle, the field synergy angle (β) can be regarded as the evaluation standard of coincidence degree of velocity direction and the temperature gradient (Guo et al., 1998). An efficient way to raise the heat sources or convection terms and enhance the heat transfer consequently is to decrease the β. This indicates that the smaller β is, the stronger heat transfer in this study (Guo et al., 2005). The definition of β is described by equation as follows:

$$cos\beta = \frac{\boldsymbol{V} \cdot grad\boldsymbol{T}}{|\boldsymbol{V}| \cdot |grad\boldsymbol{T}|} \tag{40}$$

where $\boldsymbol{V}$ denotes the velocity and $grad\boldsymbol{T}$ denotes the temperature gradient. Figure 11 presents simultaneously the distribution of Nu and β, for investigating the heat transfer characteristics inside the cavity. Generally, whether on the upstream or downstream disk wall, Nu exhibits a downward trend as the radial height increases. As a result, under the condition of Sr <1, a lower Sr presents a higher relative tangential velocity, which would result in a larger angle between the velocity direction and temperature gradient. With a higher β, the local heat transfer is weakened, manifested as the decrease of Nu. Analogically, the same phenomenon can be observed as the θ_r decreases. Owing to that, the decrease of θ_r causes the decrease of initial Sr. However, the mechanism that affects heat transfer is complicated and consists of not only the field synergy angle but also the wall jet effect. Compared with the upstream disk wall, the airflow at the low radius of the downstream disk wall quickly flowed to the upstream disk wall to form a strong convection heat transfer. Therefore, the Nu on the downstream disk wall was larger than that on the upstream disk wall.

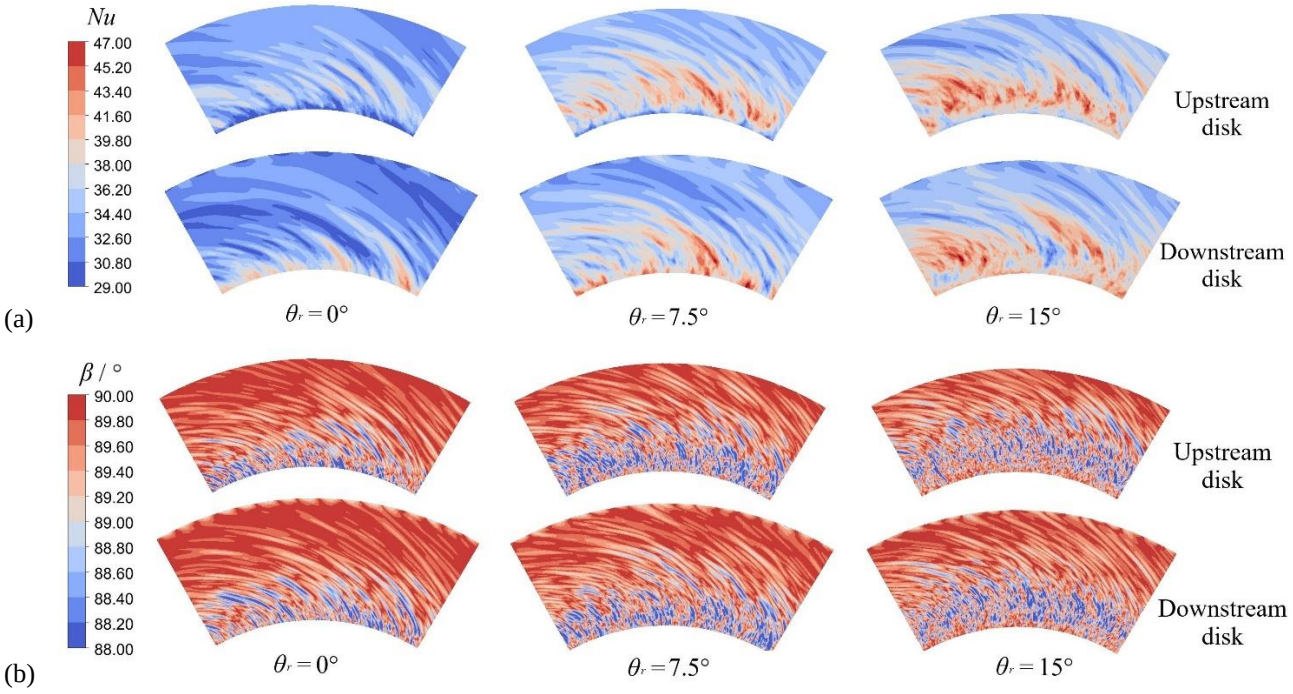

Fig. 11 (a) Distribution of Nu along radial direction on both upstream and downstream wall; (b) Distribution of β along radial direction on both upstream and downstream wall

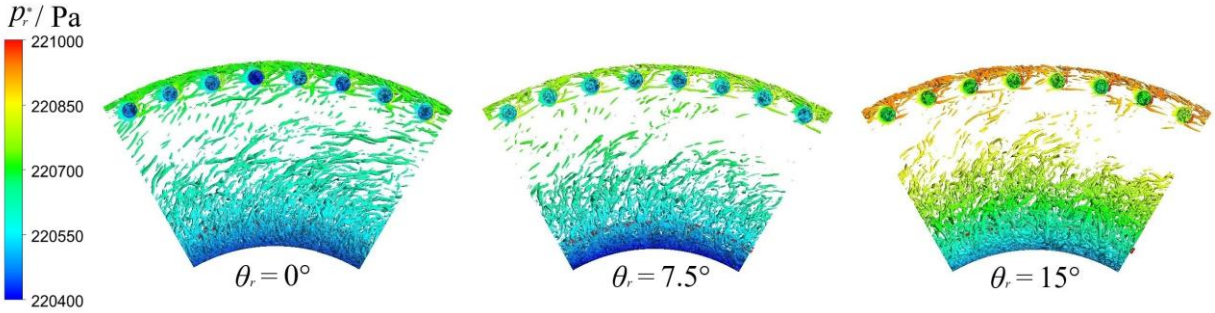

Fig. 12 Coherent structure in computational model

4.2 Unsteady Characteristics

To visualize the coherent structure, the Q-criterion was applied in this study to identify vortices as areas where the vorticity magnitude was greater than the magnitude of the rate of strain (Jeong & Hussain, 1995). Figure 12 shows the coherent structure of three models with different θ_r. Owing to the jet collision with the cavity wall, small-scale vortices were generated in the low-radius region. They move radially upward under the impact of the centrifugal force. As the radius increased, the vortices were moderately stretched in the direction opposite to the cavity rotation, resulting in the emergence of strip vortices. However, this effect is weakened with the increase of θ_r, because Sr is bigger in the cavity with model of larger θ_r, the relative rotational velocity is lower correspondingly, hence the vortex is stretched less. Therefore, an increase in c can efficiently suppress the development of low-velocity large-scale vortices in the high-radius region. Furthermore, due to that the Sr of computational model with θ_r = 15° is higher, which represents a higher tangential velocity, the high-speed large-scale vortices occupied dominant position, the viscous dissipation is weaker and the relative total pressure is higher than them of other 2 models. Overall, the flow structures inside the cavities of the three models were analogous.

For investigating the impact of θ_r on the turbulence inside the cavity, four monitoring points are set along the radial direction from high-radius region to low-radius region uniformly. The x values are 0.9, 0.8, 0.7, and 0.6. The power spectra of the velocity fluctuation inside the cavities of the three models are shown in Figs. 13(a-c). In the case of the jet collision with the cavity wall, in the low-radius region (x = 0.6), the spectrum is the highest, and the vortex energy is the maximum at this time. Furthermore, as the radius increased, the mid-frequency spectrum exhibited a decreasing trend, indicating that large-scale vortices are dissipated. Compared to the models with θ_r= 0° or 7.5°, the spectrum of the model with θ_r= 15° has distinctions. The tangential high-frequency spectrum changed along the radial direction as a result of the higher Sr. Overall, the component along the tangential direction played a significant role in dominating the flow than those along the other two directions.

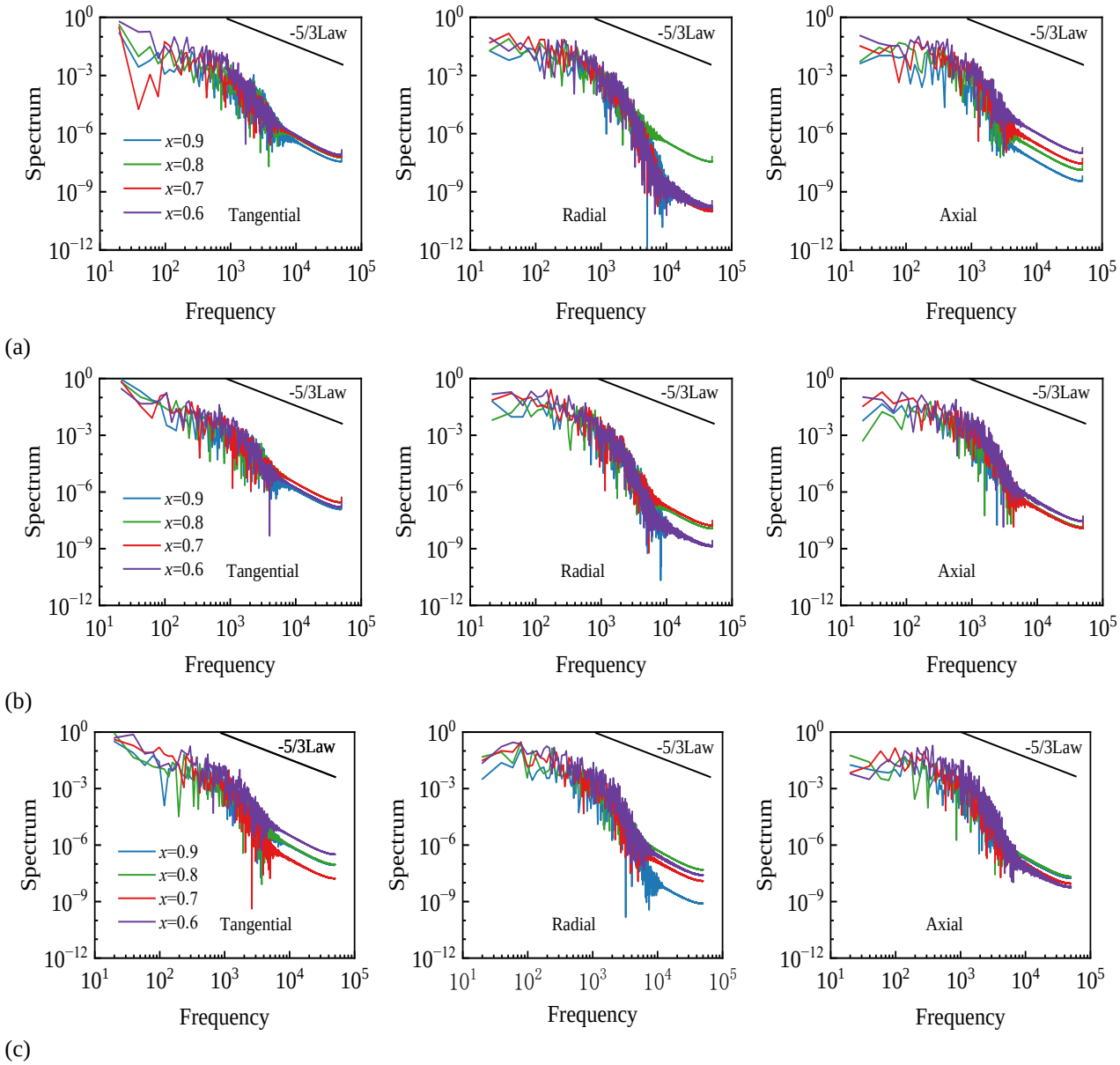

Fig. 13 Power spectrum of different computational models: (a) θ_r = 0°; (b) θ_r = 7.5°; (c) θ_r = 15°

Here, we define the turbulent heat flux (<v′T′>) as the product of the fluctuation velocity and temperature. The dimensionless axial length (X) is equal to the actual distance between the observed position and upstream disk wall divided by the distance between the upstream disk wall and downstream disk. Figure 14 shows the distribution of <v′T′> along the axial direction at different radial locations in the various models. It can be concluded that the value of <v′T′> shows relatively large fluctuations near both disk walls, which are caused by the wall jet impact. When approaching the axial intermediate region, the turbulent heat flux gradually decreases owing to the weakened fluctuation of the turbulence. Moreover, in the high-radius region, this fluctuation in <v′T′> is weakened, the heat transfer is weakened correspondingly as well. This was because the impact of the wall jet was relatively weak, and the turbulent fluctuation was restricted by the higher tangential velocity of the airflow.

Figure 15 shows the distribution of turbulent kinetic energy (TKE), which is defined as (Pope, 2000) follows:

$$TKE = \frac{(v')^2}{2} \tag{41}$$

It is shown that the value of TKE increases as the θ_r increases, particularly in the region of receiver holes outlet and the supply holes. As a result, when θ_r is relatively low, the high-speed pre-swirl jet will rapidly decelerate in the receiver holes region, causing severe local fluid mixing and emergence of high TKE. Correspondingly, larger local losses occur in this region, as shown in Fig. 9. Meanwhile, the airflow finishes the transition process from radial to axial in the supply holes and is forced to accelerate until its rotational velocity equals the rotational velocity of the co-rotating cavity, which indicates that Sr in this region would be obligatorily increased to 1. However, the inlet Sr of supply holes is lower in the model with lower θ_r, which would result in a more rapid acceleration process in this region under the condition of Sr is less than 1. Stronger velocity fluctuations and larger local losses were generated. This manifests as a decrease in p^*_{rel} as shown in Fig. 9.

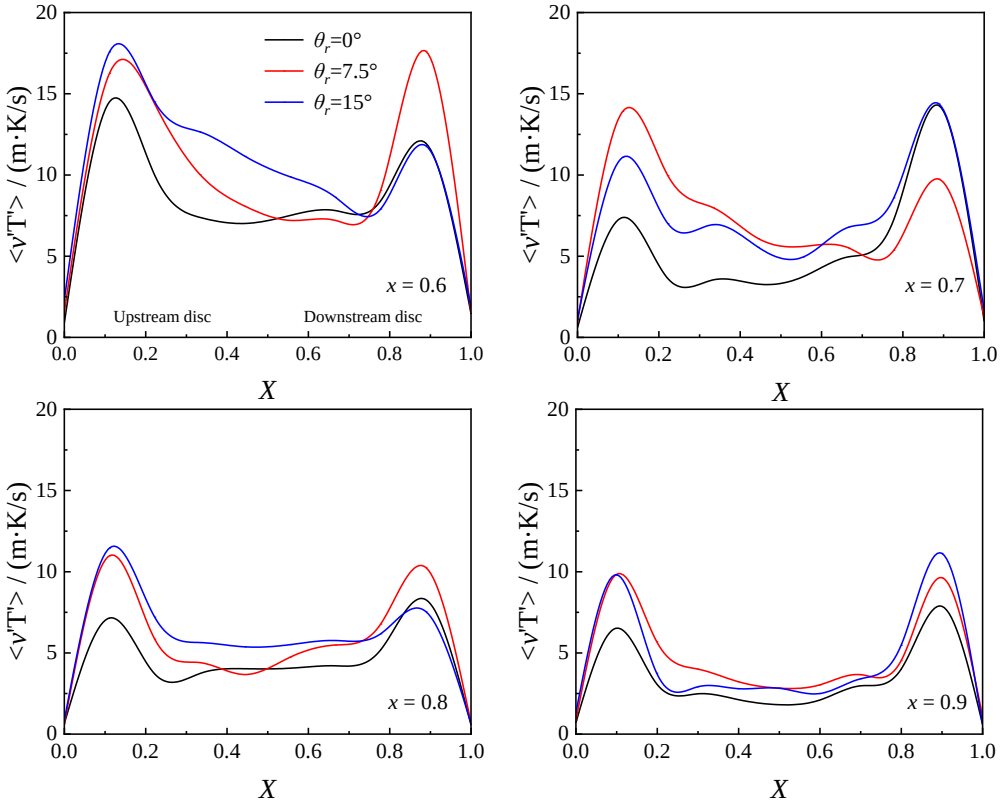

Fig. 14 Distribution of turbulent heat flux along axial direction in different radial location

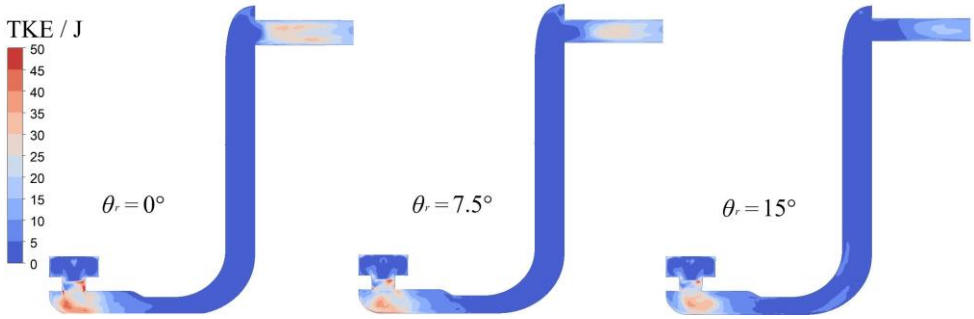

Fig. 15 Distribution of TKE

5. CONCLUSION

LES simulations were conducted to investigate the effect of the receiver hole's tangential angle on the various components of a radial pre-swirl system. A mathematical model considering the wall heat flux was developed to predict the distributions of the swirl ratio, relative total pressure, and relative total temperature inside the co-rotating cavity. The conclusions are summarized below.

1. Strong interference exists between the receiver holes, pre-rotating nozzles, co-rotating cavities, and supply holes. As the pre-swirl nozzles accelerate the jet, the receiver holes inevitably generate high local losses. An appropriate increase in the tangential angle of the receiver holes can improve the situation. Compared to receiver holes with a tangential angle of 0°, the local loss of receiver holes with a tangential angle of 15° can be reduced by 11.47%. An increase in the swirl ratio in the co-rotating cavity can reduce the turbulent fluctuation and local losses in the supply holes.

2. Increasing the tangential angle of the receiver holes can improve convection heat transfer on the disk wall surfaces. The convection heat transfer was improved again on the downstream disk wall due to the airflow on it. As the radius increases, the field synergy angle gradually increases, and the heat transfer on the disk walls gradually weakens. As the swirl ratio in the co-rotating cavity increases with the receiver hole tangential angle, the reduced relative tangential velocity reduces the field synergy angle, thereby enhancing the heat transfer on the disk walls. The turbulent heat flux exhibited a rapid fluctuation when approaching the disk walls from the axial midspan of the co-rotating cavity, owing to the wall jet impact. The development of low-velocity, large-scale vortices is restricted because the tangential angle of the receiver holes increases in the co-rotating cavity of the

pre-swirl system. Small-scale vortices were stretched along the opposite direction of the co-rotating cavity, resulting in the formation of stripe vortices in the high-radius region. Furthermore, the high-frequency spectra of low radii increased with the tangential angle of the receiver holes, strengthening the fluctuation of the tangential velocity component.

3. The development of low-velocity, large-scale vortices is restricted because the tangential angle of the receiver holes increases in the co-rotating cavity of the pre-swirl system. A large number of small-scale vortices were generated owing to the collision of the wall jet and disk wall in the low-radius region. They stretched along the opposite direction of the co-rotating cavity, resulting in the formation of stripe vortices in the high-radius region. As the receiver hole tangential angle increased, fewer stripe vortices were generated, owing to the lower relative velocity. Furthermore, the high-frequency spectra of low radii increased with the tangential angle of the receiver holes, strengthening the fluctuation of the tangential velocity component.

4. A mathematical model was developed to predict the swirl ratio, relative total pressure, and relative total temperature distributions in the co-rotating cavity. It is based on the energy equation and the linear Ekman layer equation. It shows errors of 0.15% and 0.59% compared with the LES results for the relative total pressure and relative total temperature, respectively. This demonstrated that the prediction results of the mathematical model remained highly consistent with the LES results.

To evaluate the accuracy and universality of a mathematical prediction model, groups of experimental data should be compared with the prediction results. Furthermore, this study focused on a pre-swirl system with a simple co-rotating cavity. However, co-rotating cavities with installed impellers are commonly used in engineering. The impact of receiver holes on various pre-swirl systems with different structural properties should be investigated further.

ACKNOWLEDGEMENTS

This study is supported by computational resources from Beijing Paratera Co., Ltd.

CONFLICT OF INTEREST

The authors declare no conflict of interest.

AUTHORS CONTRIBUTION

Difei Wang: Conceptualization, methodology, software, validation, formal analysis, investigation, resources, data curation, writing—original draft preparation, writing—review and editing, visualization; **Chenxi Qiu:** Conceptualization, methodology, software, validation, formal analysis, investigation, data curation; **Chi Song:** software, validation, formal analysis, investigation, resources, data curation, writing—original draft preparation, writing—review and editing, visualization; **Yifan Xu:** formal analysis, investigation; **Weicheng Wang:** formal analysis, investigation; **Platonov Ivan Mihailovich:** Conceptualization, methodology, validation, investigation, writing—review and editing.

REFERENCES

Bricteux, L., Duponcheel, M., & Winckelmans, G. (2009). A multiscale subgrid model for both free vortex flows and wall-bounded flows. *Physics of Fluids*, *21*(10). https://doi.org/10.1063/1.3241991

Cao, N., Luo, X., & Tang, H. (2022). A Bayesian model to solve a two-dimensional inverse heat transfer problem of gas turbine discs. *Applied Thermal Engineering*, *214*, 118762. https://doi.org/10.1016/j.applthermaleng.2022.118762

Chew, J. W., & Rogers, R. H. (1988). An integral method for the calculation of turbulent forced convection in a rotating cavity with radial outflow. *International Journal of Heat and Fluid Flow*, *9*(1), 37-48. https://doi.org/10.1016/0142-727x(88)90028-8

Chew, J. W., Farthing, P. R., Owen, J. M., & Stratford, B. (1989). The use of fins to reduce the pressure drop in a rotating cavity with a radial inflow. *Journal of Turbomachinery*, *111*, 349-356. https://doi.org/10.1115/1.3262279

Da Soghe, R., Bianchini, C., & D'Errico, J. (2018). Numerical characterization of flow and heat transfer in preswirl systems. *Journal of Engineering for Gas Turbines and Power*, *140*(7), 071901. https://doi.org/10.1115/GT2017-64503

Dou, H. S. (2022). *Origin of turbulence*. Energy Gradient Theory. Singapore: Springer. https://doi.org/10.1007/978-981-19-0087-7

Farthing, P. R., & Owen, J. M. (1991). De-swirled radial inflow in a rotating cavity. *International Journal of Heat and Fluid Flow*, *12*(1), 63-70. https://doi.org/10.1016/0142-727X(91)90009-K

Farthing, P. R., Chew, J. W., & Owen, J. M. (1991). The use of de-swirl nozzles to reduce the pressure drop in a rotating cavity with a radial inflow. *Journal of Turbomachinery*, *113*, 106-114. https://doi.org/10.1115/1.2927727

Firouzian, M., Owen, J. M., Pincombe, J. R., & Rogers, R. H. (1986). Flow and heat transfer in a rotating cylindrical cavity with a radial inflow of fluid: Part 2: Velocity, pressure and heat transfer measurements. *International Journal of Heat and Fluid Flow*, 7(1), 21-27. https://doi.org/10.1016/0142-727X(86)90037-8

Ghasemi, M. H., Hoseinzadeh, S., & Memon, S. (2022). A dual-phase-lag (DPL) transient non-Fourier heat transfer analysis of functional graded cylindrical material under axial heat flux. *International Communications in Heat and Mass Transfer*, *131*, 105858. https://doi.org/10.1016/j.icheatmasstransfer.2021.10

5858

Guo, Z. Y., Li, D. Y., & Wang, B. X. (1998). A novel concept for convective heat transfer enhancement. *International Journal of Heat and Mass Transfer*, *41*(14), 2221-2225. https://doi.org/10.1016/s0017-9310(97)00272-x

Guo, Z. Y., Tao, W. Q., & Shah, R. (2005). The field synergy (coordination) principle and its applications in enhancing single phase convective heat transfer. *International Journal of Heat and Mass Transfer*, *48*(9), 1797-1807. https://doi.org/10.1016/j.ijheatmasstransfer.2004.11.007

Hide, R. (1968). On source-sink flows in a rotating fluid. *Journal of Fluid Mechanics*, *32*(4), 737-764. https://doi.org/10.1017/s002211206800100x

Jeong, J., & Hussain, F. (1995). On the identification of a vortex. *Journal of Fluid Mechanics*, *285*, 69-94. https://doi.org/10.1017/S0022112095000462

Kármán, T. V. (1921). Über laminare und turbulente Reibung. *ZAMM-Journal of Applied Mathematics and Mechanics/Zeitschrift für Angewandte Mathematik und Mechanik*, *1*(4), 233-252. https://doi.org/10.1002/zamm.19210010401

Kong, X., Huang, T., Liu, Y., Chen, H., & Lu, H. (2022). Effects of pre-swirl radius on cooling performance of a rotor-stator pre-swirl system in gas turbine engines. *Case Studies in Thermal Engineering*, *37*, 102250. https://doi.org/10.1016/j.csite.2022.102250

Lewis, P., Wilson, M., Lock, G. D., & Owen, J. M. (2009). Effect of radial location of nozzles on performance of pre-swirl systems: a computational and theoretical study. *Proceedings of the Institution of Mechanical Engineers, Part A: Journal of Power and Energy*, *223*(2), 179-190. https://doi.org/10.1243/09576509JPE689

Liao, G., Wang, X., & Li, J. (2014). Numerical investigation of the pre-swirl rotor–stator system of the first stage in gas turbine. *Applied Thermal Engineering*, *73*(1), 940-952. https://doi.org/10.1016/j.applthermaleng.2014.08.054

Liao, G., Wang, X., Li, J., & Zhou, J. (2015). Numerical investigation on the flow and heat transfer in a rotor-stator disc cavity. *Applied Thermal Engineering*, *87*, 10-23. https://doi.org/10.1016/j.applthermaleng.2015.05.002

Lin, A., Liu, G., Yu, X., Chang, R., & Feng, Q. (2022). Comprehensive investigations on fluid flow and heat transfer characteristics of a high-speed rotating turbine disk cavity system of aero-engine. *International Communications in Heat and Mass Transfer*, *136*, 106170. https://doi.org/10.1016/j.icheatmasstransfer.2022.106170

Liu, G., Gong, W., Wu, H., & Lin, A. (2021). Experimental and CFD analysis on the pressure ratio and entropy increment in a cover-plate pre-swirl system of gas turbine engine. *Engineering Applications of Computational Fluid Mechanics*, *15*(1), 476-489. https://doi.org/10.1080/19942060.2021.1884600

Long, C. A. (1994). Disk heat transfer in a rotating cavity with an axial throughflow of cooling air. *International Journal of Heat and Fluid Flow*, *15*(4), 307-316. https://doi.org/10.1016/0142-727X(94)90016-7

Ma, A., Liu, F., Zhou, T., & Hu, R. (2021). Numerical investigation on heat transfer characteristics of twin-web turbine disk-cavity system. *Applied Thermal Engineering*, *184*, 116268. https://doi.org/10.1016/j.applthermaleng.2020.116268

Ma, A., Wu, Q., Zhou, T., & Hu, R. (2022). Effect of inlet flow ratio on heat transfer characteristics of a novel twin-web turbine disk with receiving holes. *Case Studies in Thermal Engineering*, *34*, 101990. https://doi.org/10.1016/j.csite.2022.101990

Ostadhossein, R., & Hoseinzadeh, S. (2024). Developing computational methods of heat flow using bioheat equation enhancing skin thermal modeling efficiency. *International Journal of Numerical Methods for Heat & Fluid Flow*, *34*(3), 1380-1398. https://doi.org/10.1108/HFF-06-2023-0355

Owen, J. M., & Pincombe, J. R. (1980). Velocity measurements inside a rotating cylindrical cavity with a radial outflow of fluid. *Journal of Fluid Mechanics*, *99*(1), 111-127. https://doi.org/10.1017/S0022112080000547

Owen, J. M., Pincombe, J. R., & Rogers, R. H. (1985). Source–sink flow inside a rotating cylindrical cavity. *Journal of Fluid Mechanics*, *155*, 233-265. https://doi.org/10.1017/S0022112085001793

Pope, S. B. (2000). Turbulent flows. *Measurement Science and Technology*, *12*(11), 2020-2021. https://doi.org/10.1017/CBO9780511840531

Shen, W., & Wang, S. (2022). Large eddy simulation of turbulent flow and heat transfer in a turbine disc cavity with impellers. *International Communications in Heat and Mass Transfer*, *139*, 106463. https://doi.org/10.1016/j.icheatmasstransfer.2022.106463

Shen, W., Wang, S., & Hou, X. (2023). Coupling mechanism of pressure and temperature in a co-rotating cavity with radial flow. *Thermal Science and Engineering Progress*, *43*, 101940. https://doi.org/10.1016/j.tsep.2023.101940

Tang, H., Deveney, T., Shardlow, T., & Lock, G. D. (2022). Use of Bayesian statistics to calculate transient heat fluxes on compressor disks. *Physics of Fluids*, *34*(5), 56108. https://doi.org/10.1063/5.0091371

Unnikrishnan, U., & Yang, V. (2022). A review of cooling technologies for high temperature rotating components in gas turbine. *Propulsion and Power Research*, *11*(3), 293-310. https://doi.org/10.1016/j.jppr.2022.07.001

Vreman, B., Geurts, B., & Kuerten, H. (1997). Large-eddy simulation of the turbulent mixing layer. *Journal of Fluid Mechanics*, *339*, 357-390. https://doi.org/10.1017/S0022112097005429

Wei, S., Mao, J., Yan, J., Han, X., Tu, Z., & Tian, R. (2020). Experimental study on a hybrid vortex reducer system in reducing the pressure drop in a rotating cavity with radial inflow. *Experimental Thermal and Fluid Science*, *110*, 109942. https://doi.org/10.1016/j.expthermflusci.2019.109942

Wei, S., Yan, J., Mao, J., Han, X., & Tu, Z. (2019). A mathematical model for predicting the pressure drop in a rotating cavity with a tubed vortex reducer. *Engineering Applications of Computational Fluid Mechanics*, *13*(1), 664-682. https://doi.org/10.1080/19942060.2019.1633411

Zhang, F., Wang, X., & Li, J. (2016a). Numerical investigation on the flow and heat transfer characteristics in radial pre-swirl system with different fillet radius at the junction of inlet cavity and nozzle. *Applied Thermal Engineering*, *106*, 1165-1175. https://doi.org/10.1016/j.applthermaleng.2016.06.117

Zhang, F., Wang, X., & Li, J. (2016b). Numerical investigation of flow and heat transfer characteristics in radial pre-swirl system with different pre-swirl nozzle angles. *International Journal of Heat and Mass Transfer*, *95*, 984-995. https://doi.org/10.1016/j.ijheatmasstransfer.2016.01.010